

3.8-Micron Photometry During the Secondary Eclipse of the Extrasolar Planet HD 209458b

Drake Deming^{1,4*}, L. Jeremy Richardson^{2†}, & Joseph Harrington^{3 ‡}

¹Planetary Systems Laboratory, Code 693, Goddard Space Flight Center, Greenbelt MD 20771 USA

²Exoplanet and Stellar Astrophysics Laboratory, Code 667, Goddard Space Flight Center, Greenbelt MD 20771 USA

³Department of Physics, University of Central Florida, Orlando FL 32816-2385 USA

⁴Visiting Astronomer at the Infrared Telescope Facility, which is operated by the University of Hawaii under Cooperative Agreement no. NCC 5-538 with the National Aeronautics and Space Administration, Science Mission Directorate, Planetary Astronomy Program

ABSTRACT

We report infrared photometry of the extrasolar planet HD 209458b during the time of secondary eclipse (planet passing behind the star). Observations were acquired during two secondary eclipses at the NASA Infrared Telescope Facility (IRTF) in September 2003. We used a circular variable filter (1.5% bandpass) centered at $3.8 \mu\text{m}$ to isolate the predicted flux peak of the planet at this wavelength. Residual telluric absorption and instrument variations were removed by offsetting the telescope to nearby bright comparison stars at a high temporal cadence. Our results give a secondary eclipse depth of 0.0013 ± 0.0011 , not yet sufficient precision to detect the eclipse, whose expected depth is $\sim 0.002 - 0.003$. We here elucidate the current observational limitations to this technique, and discuss the approach needed to achieve detections of hot Jupiter secondary eclipses at $3.8 \mu\text{m}$ from the ground.

Key words: infrared: techniques: photometric - eclipses - stars:individual: HD 209458 - planetary systems - infrared

1 INTRODUCTION

The passage of a transiting extrasolar planet behind its star during secondary eclipse has emerged as a valuable technique for measuring thermal radiation emitted by hot Jupiters. Secondary eclipse detections of hot Jupiters have been accomplished using the Spitzer Space Telescope (Charbonneau et al. 2005; Deming et al. 2005, 2006a). The spectra of hot Jupiters are predicted to exhibit prominent flux peaks near 2.2 & $3.8 \mu\text{m}$, where absorption by water vapor is minimal (Sudarsky et al. 2003; Seager et al. 2005; Fortney et al. 2006). Unfortunately, the bandpasses available from Spitzer do not sample these flux peaks in an optimal way. Spitzer has no capability at $2 \mu\text{m}$, and the IRAC filter bandpass at 3.5 and $4.5 \mu\text{m}$ (Fazio et al. 2004) overlap the $3.8 \mu\text{m}$ peak minimally.

Observing hot Jupiter extrasolar planets at 2.2 and $3.8 \mu\text{m}$ in the near future must depend on ground-based observations. Ground-based observers have attempted both photometry (Snellen 2005; Snellen & Covino 2006) and spec-

troscopy (Richardson et al. 2003) to detect the $2.2 \mu\text{m}$ peak using secondary eclipses. Recently, a tentative detection of OGLE-TR-113 at $2.2 \mu\text{m}$ was reported by Snellen & Covino (2006), with eclipse amplitude 0.0017 ± 0.0005 . Knutson et al. (2006) attempted to detect the $3.8 \mu\text{m}$ peak (L-band) of TrES-1 spectroscopically, but no investigations have yet reported photometry of hot Jupiters at $3.8 \mu\text{m}$. At this longer wavelength, thermal background emission from the telescope and terrestrial atmosphere is a major impediment. Moreover, observations in the L band are significantly affected by telluric water vapor absorption, which is notoriously variable. In addition, photometric transit searches at visible wavelengths have been significantly affected by ‘red noise’ (Pont et al. 2006), and this problem might become more severe in the infrared (IR). It is therefore of interest to explore the limits of ground-based L-band photometry for secondary eclipse detection.

In this paper we report L-band photometry during the secondary eclipse of HD 209458b. A preliminary description of these measurements was reported by Deming et al. (2006b); here we report the final results. We do not achieve a detection of the planet’s thermal emission, but we elucidate the observational limitations, and we describe improvements that will allow an L-band detection from the ground.

* E-mail: ddeming@pop600.gsfc.nasa.gov

† E-mail: richardsonlj@stars.gsfc.nasa.gov

‡ E-mail:jharry@physics.ucf.edu

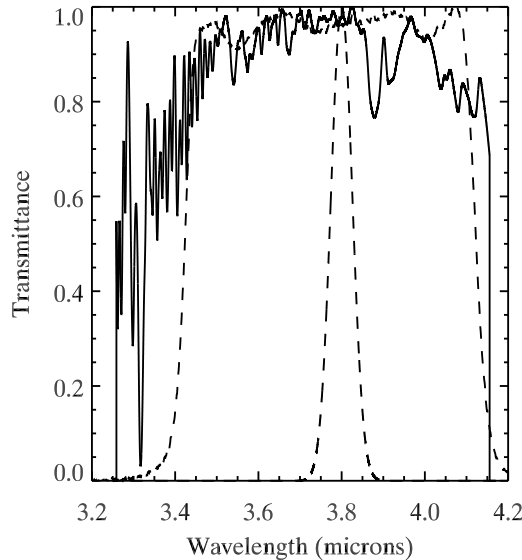


Figure 1. Telluric transmission near $3.8 \mu\text{m}$, at a spectral resolution of $\lambda/\delta\lambda = 100$, based on the transmission atlas of Livingston & Wallace (1991), shown in comparison to the standard L' bandpass (wide dashed curve), and our CVF bandpass (narrow dashed curve).

2 OBSERVATIONS

We observed HD 209458 during two secondary eclipses on 2003 September 9 & 16 UT, using NASA's 3-metre Infrared Telescope Facility (IRTF) on Mauna Kea. We also observed (and detected) a primary eclipse (transit) on 2003 August 17 UT. Since the HD 209458b transit is well observed at both visible (Brown et al. 2001) and IR wavelengths (Richardson et al. 2006), we concentrate here on the secondary eclipse observations. However, observations on the transit night were very useful in analyzing the properties of our data (see below).

We imaged HD 209458 using the 256x256-pixel NSFCam IR camera (Shure et al. 1994). To avoid detector saturation from thermal background radiation, we used a circular-variable-filter (CVF) with a 1.5% bandpass tuned to $3.8 \mu\text{m}$. This wavelength not only corresponds to a predicted peak in the planet's thermal emission, but also has optimal transmission through the terrestrial atmosphere. Figure 1 shows the CVF bandpass in comparison to the telluric transmittance at Kitt Peak, obtained by convolving the atmospheric transmission atlas of Livingston & Wallace (1991) to lower spectral resolution ($\lambda/\delta\lambda = 100$, comparable to CVF resolution). Since Mauna Kea is higher and drier than Kitt Peak, Figure 1 is a worst case representation of the telluric transmission for our observations.

It is generally not feasible to monitor comparison stars simultaneously with the target star in ground-based thermal IR photometry. Attaining the requisite wide field of view would require an increase in the per-pixel solid angle seen by the detector, to the point where the observations would be unavoidably saturated by thermal background. Instead, our observations alternated between HD 209458 and a comparison star, moving the telescope between them at the most

rapid possible cadence (17 sec for telescope motion and settling). Our imaging sequence consisted of a continuing series of exposures in the order $T_a, C_a, C_b, T_b, T_a, \dots$, where T indicates the target star (HD 209458), and C indicates a comparison star (see below). The subscripts a and b indicate two distinct nod positions on the detector array, separated by 6 arcsec (110 pixels). The nod is used for subtraction of thermal background (see Infrared Photometry section). The observations commenced each night before the time of secondary eclipse, and continued for as long as possible after eclipse.

The ideal comparison star would have an IR brightness comparable to the target, and would lie at a close angular distance. Unfortunately, no ideal star exists near HD 209458. We must choose between fainter stars in close proximity, or brighter stars at greater angular distances. Since these are exploratory observations, we elected to try both approaches. On 9 Sept we monitored HD 209346 (A2, $V = 8.3$, 0.2 degrees distant). To compensate for this star being 0.7 magnitudes fainter than HD 209458, we added additional comparison images to the observing sequence, viz.: $T_a, C_a, C_b, C_a, C_b, T_b, T_a, \dots$. On 16 Sept we monitored HD 210483 (G1, $V=7.6$, 1.7 degrees distant), following Richardson et al. (2003). For all stars, images consisted of two co-adds of 5 sec exposures. A single 5 sec exposure produced about 2×10^8 electrons of background radiation within our synthetic aperture for photometry (see below), and about 5×10^6 electrons due to HD 209458.

3 INFRARED PHOTOMETRY

Because the thermal background is intense at this wavelength, weighting the stellar image by the average point-spread-function (PSF) could in principle achieve an optimum signal-to-noise ratio (SNR) for photometry. The stellar PSF at this wavelength exhibits a significant component due to diffraction, as shown in Figure 2. Unfortunately, the PSF also contains a large contribution from seeing, and did not prove to be sufficiently stable to utilize PSF-weighted photometry. We therefore extracted photometric intensities for the star using simple aperture photometry, with a circular synthetic aperture of radius 20 pixels (1.1 arcsec). The best radius for the synthetic aperture was determined by minimizing the scatter in the photometric intensities. With radii significantly larger than 20 pixels, the greater background noise within the aperture degrades the SNR, and with significantly smaller radii the photometry becomes sensitive to seeing fluctuations.

A significant factor in the quality of our photometry is telescope focus, which changes with temperature and has to be monitored and corrected by the IRTF observer. We found that both the background level and the stellar intensity varied with telescope focus. Figure 3 shows the background level for the HD 209458 transit observations (best night to illustrate this effect). Improvements in telescope focus are accompanied by a decrease in the measured background. We attribute this to less off-axis acceptance of warm radiation from the telescope structure as focus improves. The dependence of background on observed airmass allows us to deduce that $\sim 80\%$ of the background originates from

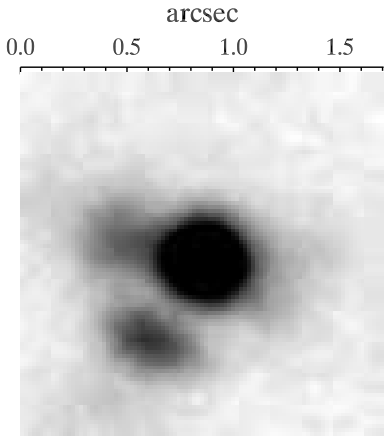


Figure 2. Background-subtracted image of HD 209458 at $3.8 \mu\text{m}$, in reverse grayscale, showing telescope diffraction effects. The image core has been saturated to illustrate the weak diffraction wings, which are asymmetric due to optical imperfections. At this wavelength the PSF is a mixture of diffraction and seeing.

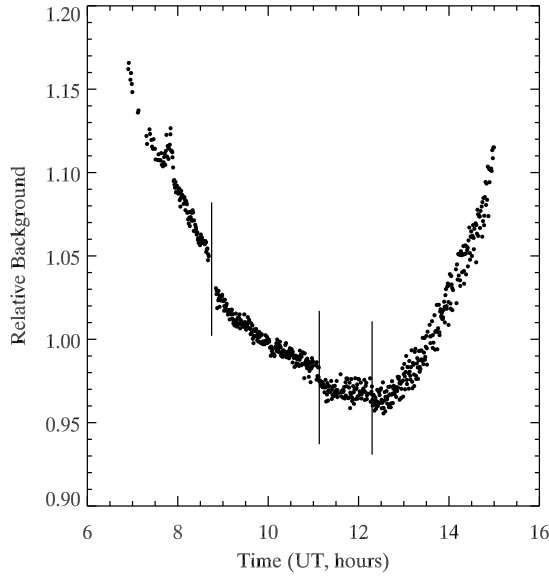


Figure 3. Thermal background intensity in our $3.8 \mu\text{m}$ bandpass, as observed on 17 August 2003. The vertical lines indicate times of telescope re-focusing, showing that the background level decreases with updates in telescope focus.

the telescope and warm optics, the remaining $\sim 20\%$ being contributed by the terrestrial atmosphere.

In principle, the stellar photometry should be independent of telescope focus, as long as the synthetic aperture is of sufficient radius to encompass slightly defocused stellar images. In practice, we find that the stellar photometric values change by $\sim 1\%$ when updating telescope focus. We

found a weak correlation between intensity and the width of the stellar PSF (correlation coefficient ~ 0.4). Broader stellar images - from poorer seeing - tended to yield less intensity from aperture photometry. Although this correlation was dominated by seeing fluctuations, we expect that imperfections in focus have a similar effect. The sense of the correlation - less photometric intensity from broader PSFs - is consistent with not recovering all of the stellar photons within a given synthetic aperture as the image broadens. Using extremely large synthetic apertures is impractical due to background noise. We therefore analyzed our data in blocks between focus updates, measuring HD 209458 relative to the comparison star.

Although thermal IR photometry is daunting in many respects, there are some compensating advantages. These include insensitivity to intra-pixel variations, and the ability to flat-field the detector array nearly simultaneously with the data acquisition. Since the thermal background will be spatially uniform over our 14 arcsec field of view, we use the thermal background for flat fielding. Within each block defined by focus updates, we compute the median image. Since telescope nods and pointing jitter move the star by significantly more than its FWHM, the median image does not contain the star, and defines an accurate flat field calibration for that data block.

We measure the intensity ratio between HD 209458 and the comparison star, and we do this separately for the 'a' and 'b' nod positions in each data block. To increase the precision of the comparison star photometry, we smooth the individual comparison measurements using a 10-point moving average. This increases the effective time scale for our HD 209458 to comparison ratio to ~ 20 minutes. We spline-interpolate the comparison star moving average to the times of the HD 209458 observations, and compute the ratio. Results from this process, for two representative data blocks, are shown in Figure 4. We explored the possibility of improving the precision by decorrelating the stellar intensities against the widths of their PSFs, but we found that the correlation was not sufficiently strong to significantly improve our results.

We compute errors for each photometric measurement of HD 209458. Both the HD 209458 photometry and the comparison star photometry contribute to the total error. The largest source of error is background shot noise, and we compute its magnitude by measuring the per-pixel fluctuations in the flat-fielded background for each frame, using the region immediately adjacent to the photometry aperture. This noise was about two times larger than the theoretical value from the square root of the electron number. Scaling the measured fluctuation as the square root of the number of pixels, we calculate the shot noise in the synthetic aperture due to background. Stellar photon noise and detector read noise are negligible by comparison. We propagate these errors through the relative photometry, and compute the error in the 10-point moving average of the comparison stars. Comparison star and HD 209458 errors are added in quadrature, yielding an average per-point fractional precision of 0.009 per single HD 209458 measurement. (In this paper we quote eclipse depths and errors in units of the stellar intensity, *not* in magnitudes.) This does not include errors due to the terrestrial atmosphere, which may not cancel perfectly between HD 209458 and the comparison star.

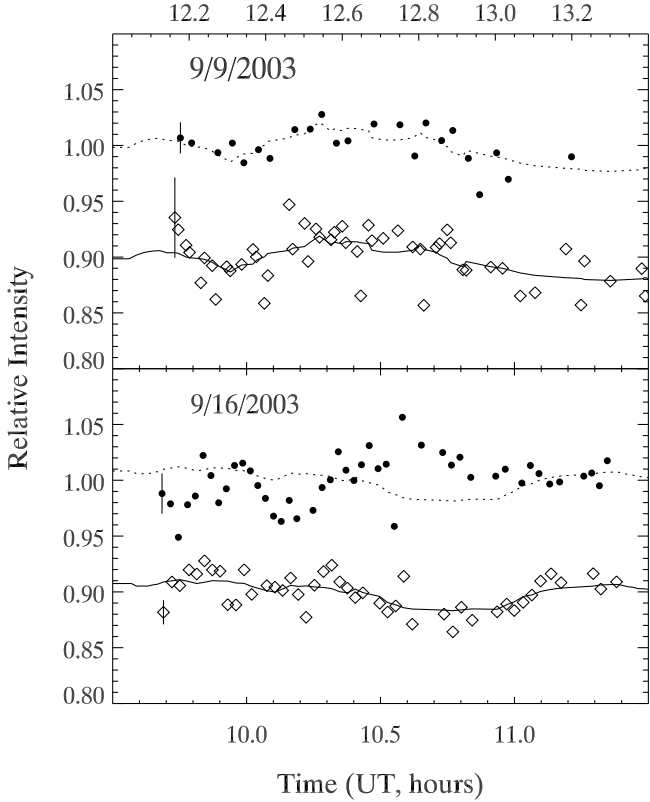


Figure 4. Sample $3.8 \mu\text{m}$ photometry UT 9 Sept 2003 (upper panel) and UT 16 Sept (lower panel). The open diamonds show observations of the comparison star (HD 209346 on 9 Sept & HD 210483 on 16 Sept). The comparison star points have been normalized to 90% of HD 209458 (solid symbols), for clarity. The solid line is a 10-point moving average of the comparison star data; the dashed line scales this relation to HD 209458. Representative error bars ($\pm 2\sigma$ for clarity, and including only background fluctuations) are plotted over the first points in each series. Note the tendency for HD 209458 to track the nearby comparison star on 9 Sept, but not the more distant comparison star observed on 16 Sept.

4 RESULTS AND DISCUSSION

Although the photometry exhibits a general decrease in intensity with increasing airmass, there are significant fluctuations on shorter time scales. Measurements of comparison stars are necessary for this reason. Examination of the photometry for the nights of 9 & 16 Sept shows much better results using the closer, albeit fainter, comparison star (9 Sept). This is obvious on Figure 4, where the lower panel (16 Sept) exhibits fluctuations on time scales of ~ 20 minutes that are not similar between HD 209458 and the comparison star. We find that this holds on 16 Sept even when fewer points are used in the moving average of this bright comparison star. Therefore, the data on this night are not useful for eclipse detection. We conclude that the relatively large angular separation between HD 209458 and HD 210483 (1.7 degrees) is the principal factor contributing to this significant degree of atmospheric noise. Physically, this probably results from incoherence of water vapor absorption over the distances separating the lines of sight to these two stars.

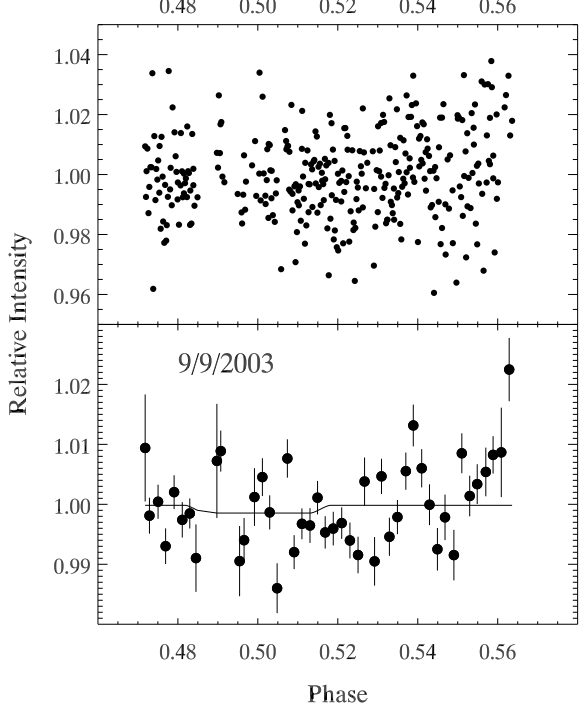


Figure 5. Results for $3.8 \mu\text{m}$ photometry of HD 209458b on UT 9 Sept 2003. Upper panel: 331 individual observations, shown without error bars for clarity. Lower panel: results in bins of 0.002 in phase, with error bars and the best-fit eclipse curve added. The best-fit eclipse depth is 0.0013 ± 0.0011 , not a significant detection.

Note that this conclusion will not necessarily apply to the results of Richardson et al. (2003), since those authors used HD 210483 to perform *spectroscopy* relative to HD 209458.

In contrast to the 16 Sept results, the data for 9 Sept (e.g., upper panel of Figure 4) show that fluctuations in HD 209458 consistently track those of HD 209346, even though the effective time scale of these data is ~ 20 minutes (10-point moving average of the comparison star). This is also true for the other data blocks on this night. The increase in thermal background per unit airmass was approximately two times lower on 9 Sept than 16 Sept (10% vs. 20%). Nevertheless, we judge that the primary difference in our results is due to the comparison star selection: a nearby, albeit faint, comparison star is more useful than a brighter but more distant one for photometry in the L-band. Certainly this is true in conditions that are less than optimum.

Figure 5 (upper panel) plots the 331 individual observations from 9 Sept versus the planet's orbital phase, using the ephemeris from Knutson et al. (2007). These data are normalized to an average of unity. The lower panel averages the data in bins of width 0.002 in phase, and adds error bars calculated as discussed above. The best-fit eclipse depth (0.0013 ± 0.0011) does not have sufficient precision for detection, but our results are similar to a result recently reported for TrES-1 by Knutson et al. (2006), who used a spectroscopic technique at $3.8 \mu\text{m}$.

The reduced chi-squared of the fit in the lower panel of Figure 5 is 1.96, consistent with a per-point scatter of 0.014 (upper panel), about 50% larger than the errors from

background shot noise. Additional error can arise from atmospheric noise that is not common to both stars on the spatial and temporal scales of these observations. This 'red noise' (amplitude ~ 0.01) can be reduced by using a broader optical bandwidth. New IR cameras such as NSFCam-2 at the IRTF can utilize the full L' band without saturating. This will increase the SNR by a factor of ~ 3.5 per image (SNR proportional to square root of optical bandwidth). Having greater SNR per frame should increase the precision of fainter comparison stars; for example, HD 209346 should improve from 0.021 to 0.006 precision in 10 seconds of integration. A more significant effect of a broader optical bandwidth is that it will decrease the temporal bandwidth of the red noise, by an order of magnitude. This follows because the time to define the target-to-comparison-star ratio to a given precision shortens as the square of the SNR per image, and we would not need to utilize a 10-point moving average for the comparison star.

Atmospheric noise power often increases as the inverse of the sampling frequency ('1/f' noise). We have calculated the improvement expected in both the background shot noise and the atmospheric 1/f noise using the full L' optical bandwidth. This calculation assumes that any high frequency contribution from the terrestrial atmosphere - similar to scintillation - does not dominate on ~ 10 to 30 second time scales at this wavelength. The result indicates that our 9 Sept final errors will decrease by a factor of two. A secondary eclipse of depth 0.002 in HD 209458 would be detected to 3.6σ significance. Moreover, the greater planet-to-star contrast of the recently discovered HD 189733 system (Bouchy et al. 2005), coupled with its brighter apparent magnitude, will lead to even more favorable detectability. We conclude that ground-based detection of photons from extrasolar planets is possible at 3.8 μm .

ACKNOWLEDGMENTS

We thank our IRTF support scientist, Bobby Bus, for his expert help in making the observations, and we are grateful to John Rayner for assistance with NSFCam and to the IRTF telescope operators for their assistance.

REFERENCES

Bouchy, F., Udry, S., Mayor, M., Moutou, C., Pont, F., Iribarne, N., da Silva, R., Illovaisky, S., Queloz, D., Santos, N. C., Segransan, D. & Zucker, S. 2005, *A&A*, 444, L15

Brown, T. M., Charbonneau, D., Gilliland, R. L., Noyes, R. W., & Burrows, A. 2001, *ApJ*, 552, 699

Charbonneau, D., Allen, L. E., Megeath, S. T., Torres, G., Alonso, R., Brown, T. M., Gilliland, R. L., Latham, D. W., Mandushev, G., O'Donovan, F. T., & Sozetti, A. 2005, *ApJ*, 626, 523

Deming, D., Seager, S., Richardson, L. J., & Harrington, J. 2006, *Nature*, 552, 699

Deming, D., Harrington, J., Seager, S., & Richardson, L. J. 2006, *ApJ*, 644, 560

Deming, D., Richardson, L. J., Seager, S., & Harrington, J., 2006b, in *Tenth Anniversary of 51 Peg-b: Status of and prospects for hot Jupiter studies*, eds. L. Arnold, F. Bouchy, & C. Moutou, Frontier Group, Paris, p. 218

Fazio, G. G., and 64 co-authors 2004, *ApJ(Suppl)*, 154, 10

Fortney, J. J., Cooper, C. S., Showman, A. P., Marley, M. S., & Freedman, R. S. 2006, *ApJ*, 652, 746

Knutson, H., Charbonneau, D., Deming, D., & Richardson, L. J. 2006, paper presented at the *Transiting Extrasolar Planets Workshop*, Heidelberg, Germany, 25-28 September, 2006

Knutson, H., Charbonneau, D., Noyes, R. W., Brown, T. M. & Gilliland, R. L. 2007, *ApJ*, 655, 564

Pont, F., Zucker, S., & Queloz, D. 2006, *MNRAS*, 373, 231

Richardson, L. J., Deming, D., & Seager, S., 2003, *ApJ*, 597, 581

Richardson, L. J., Harrington, J., Seager, S., & Deming, D. 2006, *ApJ*, 649, 1043

Seager, S., Richardson, L. J., Hansen, B. M. S., Menou, K., Cho, J. Y.-K. & Deming, D. 2005, *ApJ*, 632, 1122

Snellen, I. A. G. 2003, *MNRAS*, 363, 211

Snellen, I. A. G., & Covino, E. 2006, *MNRAS*, 375, 307.

Shure, M. A., Toomey, D. W., Rayner, J. T., Onaka, P. M., & Denault, A. J. 1994, *SPIE*, 2198, 614

Sudarsky, D., Burrows, A., & Hubeny, I. 2003, *ApJ*, 588, 1121

Livingston, W., & Wallace L. 1991, *Atlas of the Solar Spectrum in the Infrared from 1850 to 9000 cm^{-1}* , National Solar Observatory, Tucson